JOURNAL OF AIRCRAFT
Vol. 40, No. 5, September–October 2003

Computational Simulation and Experimental Measurements for a Delta Wing with Periodic Suction and Blowing

Russell M. Cummings,* Scott A. Morton,† and Stefan G. Siegel‡
U.S. Air Force Academy, U.S. Air Force Academy, Colorado 80840

The low-speed, laminar flowfield for a 70-deg sweep delta wing is investigated. Solutions to the unsteady, three-dimensional, compressible Navier–Stokes equations were obtained on an unstructured grid to match results from an experiment performed in a water tunnel. The experiment was conducted with the delta wing at an angle of attack of 35 deg and the freestream flow at a root-chord Reynolds number of 4.07×10^4. Particle image velocimetry measurements were made for the flowfield while periodic suction and blowing was taking place along the delta wing leading edge. The computational results are analyzed and compared with the experimental results to show how computations and experiments can be conducted in a synergistic fashion. Details about the primary vortex location, vortex burst, secondary vortex, and shear layer interaction are shown and discussed.

Nomenclature

b	=	local wing span
C_μ	=	oscillatory momentum coefficient, $2(H/c)(\langle v' \rangle / U_\infty)^2$
c	=	wing root chord, 298 mm
F^+	=	nondimensional frequency, fc/U_∞
f	=	frequency
H	=	forcing slot height, 1.5 mm
M	=	Mach number
Re	=	Reynolds number, $U_\infty c/\upsilon_\infty$
Sr	=	Strouhal number, fc/U_∞
T	=	period of blowing and suction cycle, 1.352 s
t	=	time
U_∞	=	freestream velocity, 0.126 m/s
u, v, w	=	velocity components along x, y, and z axes
$\langle v' \rangle$	=	rms amplitude of blowing velocity
x, y, z	=	Cartesian coordinates fixed to the wing
α	=	wing angle of attack, 35 deg
υ	=	kinematic viscosity
∞	=	freestream conditions

Introduction

THE need to improve fighter aircraft and missile maneuverability has inspired extensive study of the flow past a variety of geometries, including delta wings and fuselage forebodies (Refs. 1 and 2, for example). In addition, numerous studies have centered on methods to delay or control vortex breakdown, which include a variety of blowing, suction, and various combinations of other pneumatic flow control concepts.[3–8] In recent years, the efficacy of oscillatory flow excitation with zero net mass flux and nonzero momentum flux has been shown. Oscillatory flow excitation is more effective for delaying separation from a lifting surface or promoting reattachment of initially separated flow, relative to steady blowing methods traditionally used for this purpose.

Guy et al.[9–12] and Morton et al.[13] have recently experimented with oscillatory flow excitation at the leading edge of a delta wing. They have investigated the spatial effects of periodic suction and blowing (PSB) on delta wing vortex breakdown by wind-tunnel and water-tunnel experimentation. The investigation focused on extending the aerodynamic envelope of a 70-deg sweep delta wing by active control of the vortical flow over the wing. It was shown that PSB delays vortex breakdown and wing stall and increases lift at high angles of attack. Key control parameters were defined and optimum values of these parameters were established. The experimental investigation indicates that PSB delays vortex breakdown by approximately 0.2 chord lengths, delays stall by approximately 10 deg, and increases lift by 40% at an angle of attack of 40 deg.

Following these encouraging results, a continuation of the research was undertaken at the U.S. Air Force Academy. It was aimed at giving an in-depth understanding of the mechanism through which PSB affects the structure and behavior of the leading-edge vortex. A first step in this direction was taken by Morton et al.,[13] who numerically simulated the flow about a delta wing with and without PSB. More recent studies have also been conducted in a water tunnel at the U.S. Air Force Academy, which form the basis for this paper.[14] The purpose of this investigation is to determine how well numerical simulations of the delta wing flowfield with and without leading-edge blowing and suction can match experimental measurements. Specifically, the eventual goal is to show how computations can aid in improving the experimental method by giving insight into details about the flowfield that can aid experimentalists in designing their measurements to best take advantage of limited apparatus and time.

Computational Method

The unstructured flow solver Cobalt was chosen because of its speed and accuracy; Cobalt is a commercial version of Cobalt_{60}. Cobalt solves the compressible Navier–Stokes equations, including an improved spatial operator and improved temporal integration. The code has been validated on a number of problems, including the Spalart–Allmaras model.[15] Tomaro et al.[16] converted Cobalt_{60} from explicit to implicit, enabling Courant–Friedrichs–Lewy numbers as high as one million. Grismer et al., then parallelized the code, yielding a linear speedup on as many as 1024 processors.[17] Forsythe et al.[18] provided a comprehensive testing and validation of the Reynolds-averaged Navier–Stokes models, including the Spalart–Allmaras, Wilcox k–ω, and Menter turbulence models.

A previous numerical study computed the flow over a flat-plate, semispan delta wing with a leading-edge sweep of 70 deg and

Presented as Paper 2003-1102 at the 41st Aerospace Sciences Meeting and Exhibit, Reno, NV, 6 January 2003; received 10 January 2003; revision received 16 June 2003; accepted for publication 16 June 2003.

*Distinguished Visiting Professor, Department of Aeronautics, on leave Professor, Aerospace Engineering Department, California Polytechnic State University, San Luis Obispo, CA. Associate Fellow AIAA.

†Associate Professor, Department of Aeronautics. Associate Fellow AIAA.

‡Postdoctoral Researcher, Department of Aeronautics. Member AIAA.

a 25-deg bevel on the lower surface in a wind-tunnel.[19,20] The wing had a root chord of 0.74 m with a 3-mm slot extending the entire length of the leading edge. The results of the wind-tunnel experiment showed a significant impact of periodic blowing and suction, which led to additional experiments in a water-tunnel and eventually to a desire to model numerically the water tunnel experimental results.

Solutions to the unsteady, three-dimensional, compressible Navier–Stokes equations with a laminar-flow assumption were obtained on two unstructured grids; details for the study may be found in Ref. 21. Grids from the wind-tunnel computations were first modified to match the water-tunnel model root chord of 0.298 m. A semispan coarse grid was used that contained 133,000 points and 591,000 cells, and the fine grid contained 252,000 points and 1.24 million cells. Approximately 10% of each grid was made up of prisms near the surface, whereas the remaining cells were tetrahedra. Results from both grids will be shown and discussed. Solutions were obtained at an angle of attack $\alpha = 35$ deg, with and without PSB through the leading-edge slot. Blowing and suction was applied normal to the leading edge and parallel to the upper surface of the wing from a slot of height $H = 1.5$ mm. The experimental free stream velocity was 0.126 m/s, and the corresponding root-chord Reynolds number was 4.07×10^4. The freestream Mach number for the computations was set to $M_\infty = 0.1$, with the freestream pressure and temperature chosen to match the Reynolds number of the experiment. Periodic blowing and suction was applied at a nondimensional frequency of $F^+ = 1.75$, and the momentum coefficient was $C_\mu = 0.004$. These values matched those used in the water-tunnel experiment. The grids were used to obtain solutions for the case without blowing after running the solution for 4000–5000 iterations to ensure that all start-up instabilities were damped out. The periodic blowing and suction solutions were started from the well-established nonblowing solutions.

Experimental Setup

A flat-plate delta wing with a leading-edge sweep of 70 deg and a 25-deg bevel on the lower surface was investigated in the U.S. Air Force Academy 38×110 cm free-surface water tunnel. The wing has a chord length of 298 mm, is hollow, and has a 1.5-mm slot along its leading edge. The wing was sting mounted and placed inverted at an angle of attack of 35 deg in the water tunnel.

To perturb the shear layer originating at the leading edge of the delta wing, a semispherical rubber cap was used as an oscillatory blowing and suction flow actuator. It was moved back and forth by a connecting rod, eccentrically mounted on a disk that was driven by a 560-W dc motor. The water displacement produced by the moving cap was channeled through a tube 2 cm in diameter to the hollow wing and to the length of the slot in its leading edge. With this setup, as with any oscillatory flow control method, fluid is drawn into the actuator over half of the sinusoidal cycle and ejected over the other half ($V = V_o \sin \omega t$). The phase during the forcing cycle is determined by the position of the rotating disk flywheel, which features an adjustable optical pickup to synchronize the data acquisition with a particular phase of the forcing cycle. A forcing cycle starts at 0 deg with the blowing phase, which extends to 180 deg. The suction portion between 180 and 360 deg completes the cycle.

To sample the flow, a Dantec flowmap two-component particle image velocimetry (PIV) system with a New Wave Gemini 125-mJ Nd:Yag laser operating at 532 nm was used. A Kodak Megaplus ES 1.0 charge-coupled device camera (1000×1000 pixel resolution) was mounted downstream of the delta wing, to visualize the flow in a plane perpendicular to the model suction surface. A special plexiglass viewing box was used to facilitate viewing of planes perpendicular to the wing, avoiding the inherent refraction from the water surface. For measurements in a plane at a constant spanwise location, the laser was set up below the test section illuminating the flow from below, while the camera imaged the flow through the side window.

The operating parameters for the PIV system were kept constant throughout the study. Seeding was provided using 20-μm polyethylene particles. The system operated in cross correlation mode using two images, which were correlated in the frequency domain. Before correlation, a 3×3 low-pass filter was used to widen the particle images. A 32×32 pixel interrogation area was used, and the images were processed with 75% overlap, yielding a raw vector field of 123×123 vectors. The vector acceptance criteria were a peak ratio of at least 1.2 and 25% maximum velocity variation from neighboring vectors.

PIV images were phase referenced to the forcing mechanism, to allow phase averaging of 10 images, thus, increasing signal-to-noise ratio of the data. Data sets were obtained every 10 deg through the 360-deg forcing cycle. Basic data reduction was done using the Flowmap PIV software for vector validation, spatial moving average smoothing in a 3×3 vector area and averaging of the 10 data sets. The data were then imported into LabVIEW-based postprocessing software for further data reduction and analysis. Details of the results of this study may be found in Ref. 14.

Results and Discussion

Spatial and Temporal Convergence Study

To determine the appropriate grid density and time step for the numerical simulations, a study was carried out for the highly unsteady flowfield caused by the burst vortices above the delta wing at $\alpha = 35$ deg. Details about the convergence study may be found in Ref. 21. Solutions for the delta wing using the coarse grid were obtained at various time steps, including $\Delta t = 0.020, 0.010, 0.005$, and 0.0025. The power spectrum density (PSD) of the normal force from the coarse grid solutions were obtained using MATLAB® and plotted in Fig. 1. The four time steps shown each produced a different primary frequency (shown as the wave number, which is the inverse of the Strouhal number). Clearly, the dominant unsteady features of the flow are not properly resolved if each time step yields a different vortex frequency. To determine whether or not a converged time step is being approached, the log of the wave number for each time step is plotted against the log of the time step in Fig. 2. Notice that a secondary frequency becomes apparent as the time step is decreased; the cause of the secondary frequency will be discussed later. Although the smallest time steps show convergence, the coarseness of the grid probably will not allow for all flow features to be captured.

A similar study was then conducted using the fine grid. PSDs for four of the time steps (starting with values comparable to those used for the coarse grid) are shown in Fig. 3. The computations were all performed for the same physical time (10 s) by varying the number of iterations for each time step (2500 iterations for $\Delta t = 0.004$, 5000 iterations for $\Delta t = 0.002$, etc.), and each computation was completed with two Newton subiterations. The detail of the frequency spectrum is more complex for the fine grid when compared with the coarse grid, as evidenced by multiple power spikes in the vicinity of the primary frequency. (Compare Fig. 3 with Fig. 1.)

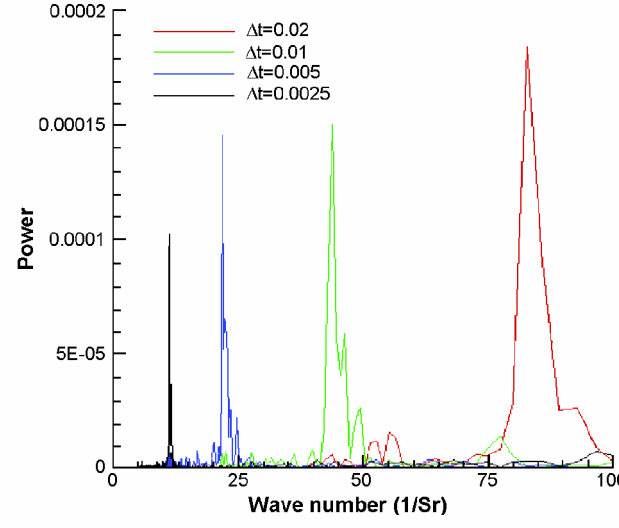

Fig. 1 PSD for coarse grid at various time steps.

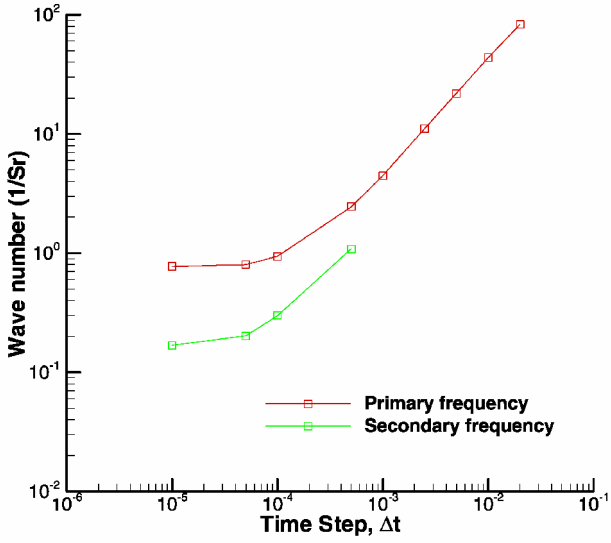

Fig. 2 Wave number variation with time step for the coarse grid.

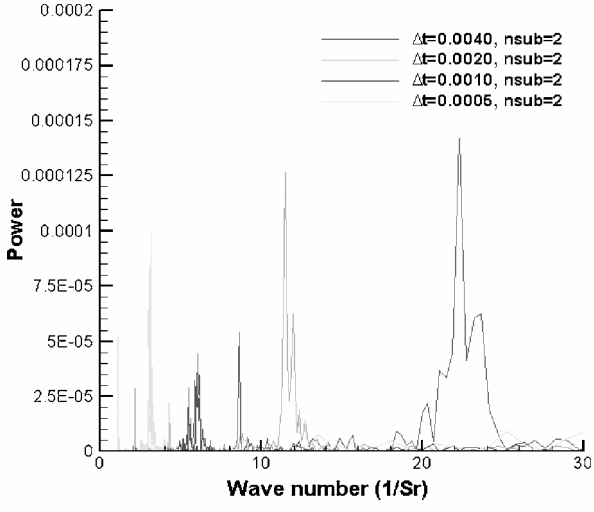

Fig. 3 Power spectrum density for fine grid at various time steps and two Newton subiterations.

These results are consolidated and shown as a function of time step and number of subiterations in Fig. 4. As can be clearly seen, both the primary and secondary frequencies converge to a constant value as the time step decreases. In addition, the converged frequencies are the same as those achieved with the coarse grid (Fig. 2), which means that the fine grid resolution is more than adequate for resolving the essential features of the flowfield. A notable feature is that the nondimensional frequency of the blowing and suction is 1.75 (which corresponds to a wave number of 0.571), which lies between the primary and secondary frequencies for the nonblowing flowfield; the flow features associated with the blowing should, therefore, be well modeled with this grid and time step.

An additional time convergence study was then performed to determine the effect of the number of Newton subiterations on the solution. Figure 4 also shows the wave number for five Newton subiteration levels ($n_{\text{sub}} = 1$, 2, 3, 4, and 5), all at a time step of $\Delta t = 0.00005$. Once again, two dominant frequencies can be seen, with the wave number for both the primary and secondary frequencies decreasing with increasing number of Newton subiterations. In fact, the secondary frequency seems to have nearly converged, although the primary frequency is very nearly converged at $n_{\text{sub}} = 4$. These studies (time step and Newton subiteration) have shown that the essential features of the flowfield are appropriately modeled with a time step of $\Delta t = 0.00005$ and a Newton subiteration level of $n_{\text{sub}} = 3$. All remaining comparisons for nonblowing cases will be made for computations made at these conditions. Certainly, slightly

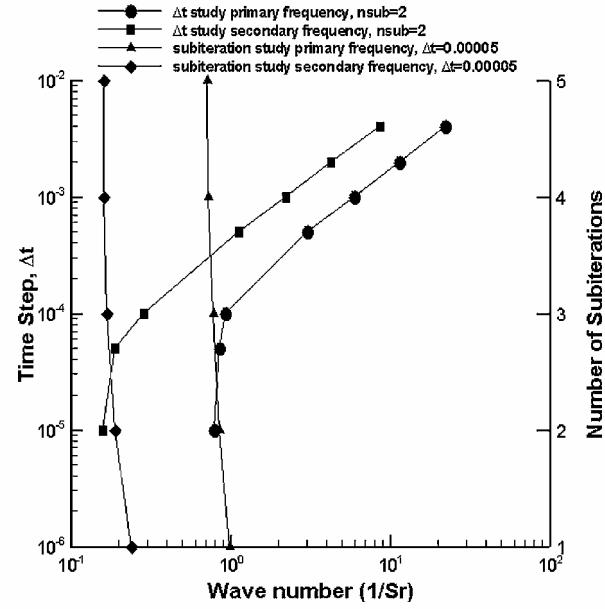

Fig. 4 Wave number variation with time step and number of subiterations for fine grid.

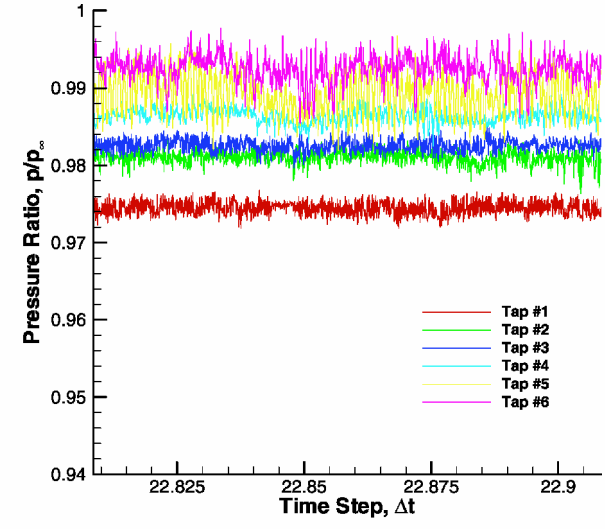

Fig. 5 Numerical prediction pressure histories along the core of the primary vortex (tap 1 is closest to delta wing vertex).

improved solutions would be obtained by using $\Delta t = 0.00001$ and $n_{\text{sub}} = 3$; these conditions are used for the following PSB cases. Using these values the flow exhibits a primary frequency of approximately 1.3 and a secondary frequency of approximately 6.0. The following discussions will attempt to determine the causes of these frequencies.

Primary and Secondary Vortex Frequencies

To determine the cause of the frequencies seen in Fig. 3, pressure taps were placed in the computational flowfield along the cores of the primary and secondary vortices. In both cases, the taps were located both before and after observed breakdown locations. Figure 5 shows the frequency history for six pressure taps along the core of the primary vortex, and Fig. 6 shows the frequency history for six pressure taps along the secondary vortex. Tap 1 is located nearest to the vertex of the delta wing, and tap 6 is beyond the vortex breakdown location. (See Table 1 for the longitudinal locations of the pressure taps.)

As can be seen in Fig. 5, the pressure frequencies increase in average values as the tap locations move further aft, showing the adverse pressure gradient normally seen on the upper surface of a wing. The frequency content at each tap location also changes with

Table 1 Longitudinal location of numerical pressure taps

Tap	Primary vortex tap x/c	Secondary vortex tap x/c
1	0.0196	0.0192
2	0.1655	0.1412
3	0.1812	0.1774
4	0.2713	0.1812
5	0.3350	0.3350
6	0.3668	0.3624

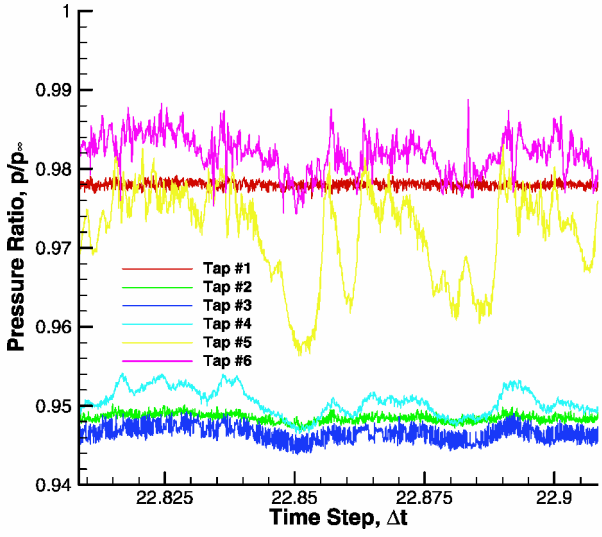

Fig. 6 Numerical prediction pressure histories along the core of the secondary vortex (tap 1 is closest to delta wing vertex).

tap position as well. There is no dominant frequency for the first three pressure tap locations on the primary vortex (taps 1–3). However, a PSD analysis of the pressure variations for taps 4–6 showed that the primary nondimensional frequency is approximately 8.5. After breakdown, a different pressure history is seen, with the primary nondimensional frequency decreasing to approximately 1.35. These frequencies were confirmed with animations of the flowfield and match the shedding evident from the leading edge and the winding of the vortex after breakdown ($F^+ = 1.35$).

Figure 6 shops the pressure histories along the secondary vortex. The most forward tap (tap 1) along the secondary vortex shows pressures that are comparable to those seen in the primary vortex (compare tap 1 in Fig. 6 with tap 1 in Fig. 5.) However, as the secondary vortex passes through tap 2–4, there is a fairly significant drop in pressure. This pressure drop is also accompanied by a noticeable instability in the pressure. The instability becomes more evident as the flow passes from tap 2 to tap 4. Finally, a noticeable difference can be seen as the flow reaches taps 5 and 6. The flow has become more chaotic, with large variations in pressure. PSD analysis shows that tap 4 has a strong frequency spike at $F^+ = 8.5$, which matches well with the frequencies found on the primary vortex. Taps 5 and 6 do not show any single, dominant frequency, however. When movies of the flowfield are viewed, it becomes apparent that the secondary vortex dissipates quickly and is diffused into the surrounding fluid, which may explain the lack of dominant frequencies at taps 5 and 6.

When this information is coupled with the flowfield visualization in Fig. 7, the results become more clear. Whereas the primary vortex breaks down and winds at an easily verifiable nondimensional frequency of $F^+ = 1.35$, the secondary vortex also breaks down; in fact, the secondary vortex breakdown location is forward of the primary vortex breakdown. This seems to suggest that the secondary vortex breakdown, and whatever may be causing it, is actually causing or affecting the primary vortex breakdown. This phenomenon has been previously observed in water-tunnel experiments.[22] Figure 8 shows the results of the water-tunnel test on a blade wing at $\alpha = 27$ deg, clearly showing the secondary vortex bursting well upstream of the primary vortex.

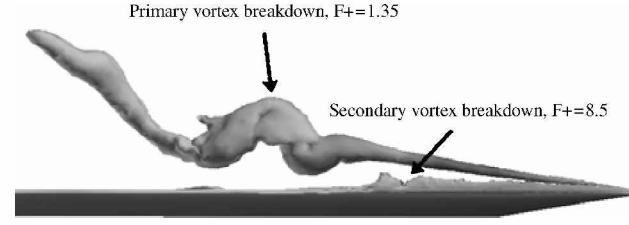

Fig. 7 Secondary vortex breakdown and secondary frequency.

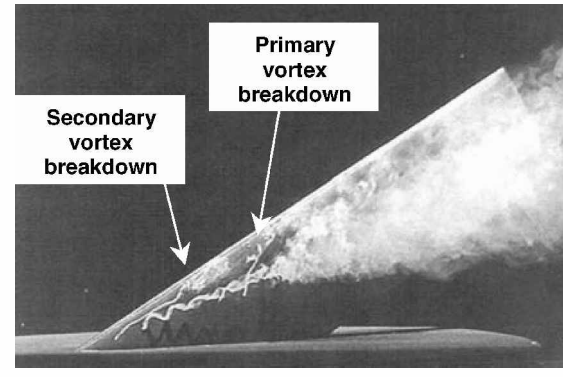

Fig. 8 Interaction between secondary vortex and primary vortex (from Ref. 22).

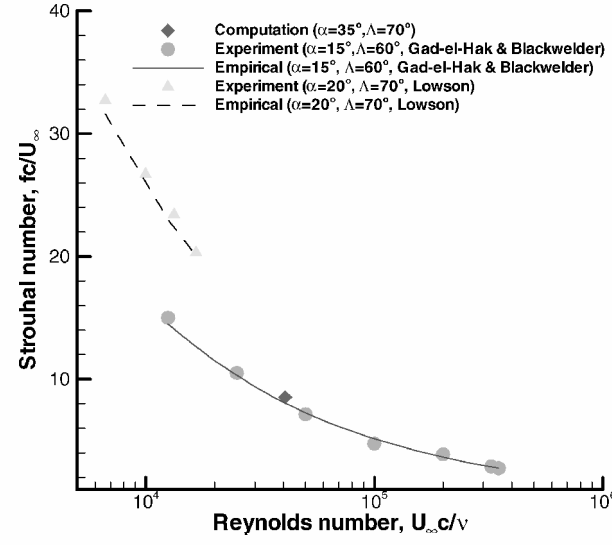

Fig. 9 Comparison of numerically predicted leading edge shedding frequency with experimental data and empirical relationships (experimental data from Refs. 23 and 24).

Wing Leading-Edge Shedding Frequency

Delta wing leading-edge shedding has been studied by, among others, Gad-el-Hak and Blackwelder,[23] who used a 60-deg delta wing, and Lowson,[24] who used a 70-deg delta wing. Both of these studies resulted in collection of the Kelvin–Helmholtz shedding frequency data as a function of flow speed, as well as the creation of empirical curve fits of the Strouhal number for the shedding frequency. Gad-el-Hak and Blackwelder[23] obtained a relation based on data collected between Reynolds numbers between 1.25 and 3.5×10^4,

$$fc/U_\infty = 1625/\sqrt{Re} \tag{1}$$

and Lowson[24] obtained data for Reynolds numbers between 6.64×10^3 and 1.66×10^4,

$$fc/U_\infty = 2577/\sqrt{Re} \tag{2}$$

The experimental data and empirical curve fits are shown in Fig. 9. Although the present computations are for a delta wing with a 70-deg

sweep angle (which matches Lowson's experiment), the angle of attack is higher than either of the experimental results. Gad-el-hak and Blackwelder noted that the shedding frequency was not a function of leading-edge sweep angle or leading-edge shape, but did find that the frequency was a weak function of angle of attack, with the frequency decreasing with α. The computational leading-edge shedding frequency Strouhal number of approximately 8.5 compares well with the experimental results. This frequency matches the frequency of the secondary vortex breakdown observed earlier.

Cause of Secondary Frequency

The secondary frequency predicted with both the coarse and fine grids (Figs. 1 and 3, respectively) was assumed to be caused by the breakdown of the secondary vortex. This breakdown takes place at approximately the same longitudinal location as the primary vortex breakdown (actually slightly ahead, as seen in Fig. 7), but with a frequency approximately five times higher than the frequency caused by the primary vortex windings. Note that the frequency information used in this analysis was taken from the integrated normal force acting on the delta wing, with the primary frequency being caused by the wound vortical structures of the primary vortex as they convect downstream beyond the breakdown location. The pressure taps resulted in a frequency of approximately $F^+ = 8.5$, slightly higher than the value of $F^+ = 6$ found from the integrated normal force predictions.

Further investigation showed that the secondary vortex breakdown is actually directly related to the leading-edge shear layer instability. Figure 10 shows the interaction between the shear layer, the secondary vortex, and the primary vortex, including the primary vortex burst location. The fingers of the shear layer instability directly match the flow structures in the secondary vortex breakdown region as seen in Fig. 7. The visualizations shown here (Figs. 7, 8, and 10) help to explain the interaction of the various portions of the flowfield: The leading-edge shedding frequency interacts with both the primary and secondary vortex, causing the secondary vortex to breakdown. The instability of both the shear layer shedding and the secondary vortex breakdown appear to interact with the primary vortex and contribute to the breakdown of that vortex. Certainly, no absolute cause and effect relationships can be deduced by the results shown earlier, but the evidence seems strong that the three flow structures are inextricably linked.

PSB

Details of the flowfield during PSB are now presented. For more information on the flowfield results without suction and blowing see Ref. 25. The vortex breakdown location without suction and blowing is presented in Fig. 11 from both the experimental data and the numerical simulation. The similarities between the two sets of results are quite good, with vortex breakdown clearly present at about 40% of chord for both the experiment and computations.

The experiment modeled the PSB as given by

$$V = V_o \sin(\omega t) \tag{3}$$

Fig. 10 Interaction between shear layer, secondary vortex, and primary vortex.

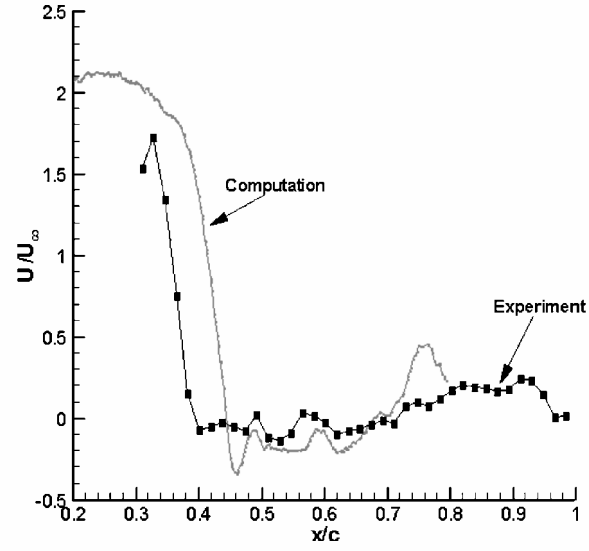

Fig. 11 Computational and experimental axial velocity development along the vortex core (unforced).

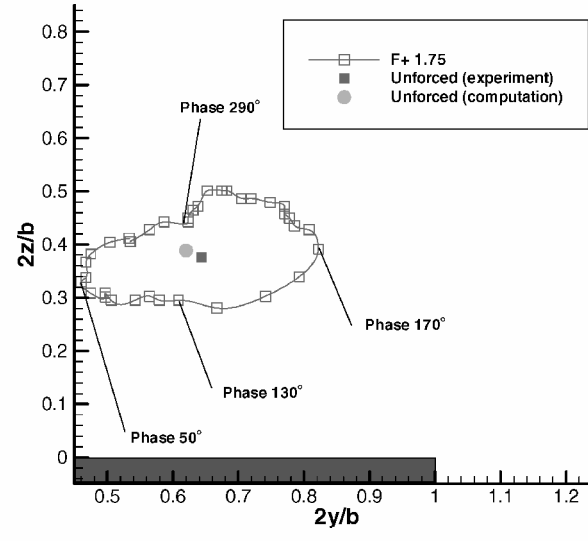

Fig. 12 Experimental location of main vortex center during the forcing cycle, $x/c = 0.4$, phase averaged data over 10 forcing cycles.

The flowfield that results from this disturbance is hopefully altered in such as way as to increase the lift on the delta wing at high angles of attack. Once the PSB is begun the primary vortex begins to move around as vortices created by the suction and blowing interact with the primary vortex. The experimental location of the primary vortex center throughout a forcing cycle is shown in Fig. 12. Also included is the computational result for the no PSB location of the vortex core. The vortex core location was determined using an algorithm contained with Fieldview postprocessing software. The location matches the experimental value to within 4% of the local wing span, which we consider to be a very good simulation. The unforced vortex core location was taken from a single time step in the solution, and because the $x/c = 0.4$ axial plane is very near to the point of vortex burst, this location of the vortex core in the computations is unsteady.

Figure 13 shows the change in the vortex at $x/c = 0.4$ as a function of the blowing cycle. Recall that a phase of 90 deg represents full blowing, whereas a phase of 270 deg represents full suction. During the blowing phase, the leading-edge shear layer is canted to the right, and the vortex core is drawn to the right. Evidence of a shear layer vortex forming is evident as well. By the time the suction phase has reached its peak, the vortex core has moved back to the left because the shear layer is no longer being affected by the suction to any great extent.

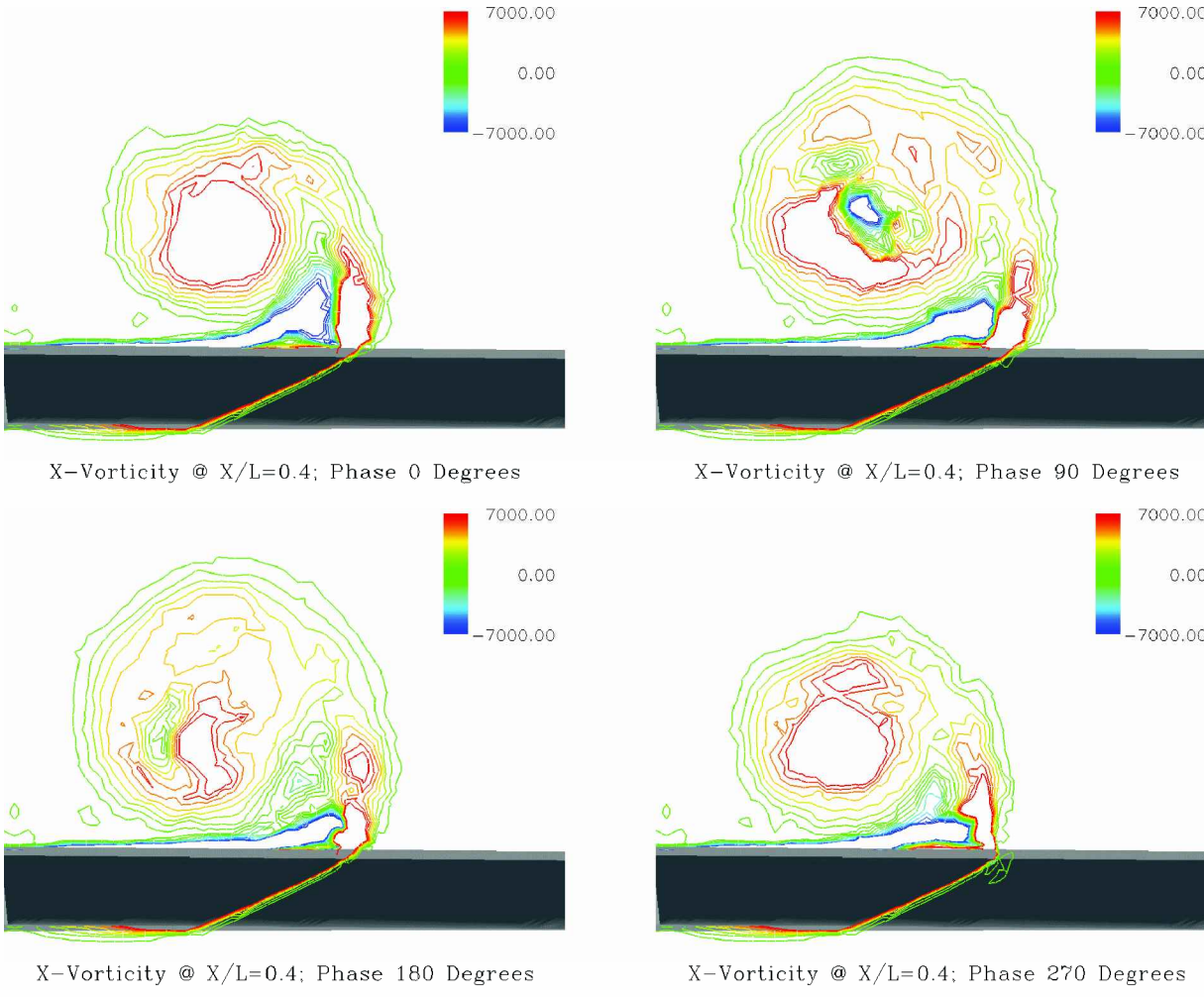

Fig. 13 Computational prediction of vortex during the forcing cycle, $x/c = 0.4$.

The experimental velocity along the vortex core shown in Fig. 14 indicates that for the unforced case a stagnant or slightly reversed flow develops around $x/c = 0.4$. This coincides with the location at which the vorticity in the unforced flow drops, between $x/c = 0.4$ and 0.5. For the forced flow, however, the location of a drop in axial velocity is dependent on the phase within the forcing cycle. For two of the phase angles investigated, 130 and 170 deg, no stagnant flow can be observed over the entire wing. At these phase angles, the shear layer vortex generated by the forcing is present in the flow. In the absence of the shear layer vortex, at phase angles of 50 and 290 deg, the forced flow does show a significant drop in axial velocity, at locations of $x/c = 0.45$ and 0.55, respectively. One possible explanation for this behavior is that the shear layer vortex entrains fluid with high axial momentum from outside the wake left from the main vortex breakdown and, thus, increases the axial velocity. This would explain the decreased surface pressure found by Guy et al., extending well downstream of their observed vortex breakdown location of $x/c = 0.75$.

The experimental velocity profiles normal to the wing surface shown in Fig. 15 indicate that at $x/c = 0.60$ the axial velocity near the wing surface is higher even for phase angles (50 and 290 deg) in which a large decrease in axial velocity can be found upstream of this location. Although the decrease in axial velocity is almost as large or even larger than for the unforced case, it is shifted about 0.05 chords away from the wing surface. Therefore, higher velocity fluid is close to the wing, increasing the local velocity and presumably decreasing the surface pressure. This explains the total increase in normal force found in previous studies.

One of the purposes of conducting a numerical simulation of PSB is to determine information that would be unavailable in most experimental settings. The PIV experiment determined a great deal of information but the computational results add to that information, and perhaps better inform future experiments. Figure 16 shows cross-flow planes at $x/c = 0.6$, which adds to the understanding of the experimental results in Fig. 15. The blowing phase of the PSB cycle is able to reestablish the primary and secondary vortex structure to some extent, enabling the higher velocity fluid to remain closer to the surface of the wing.

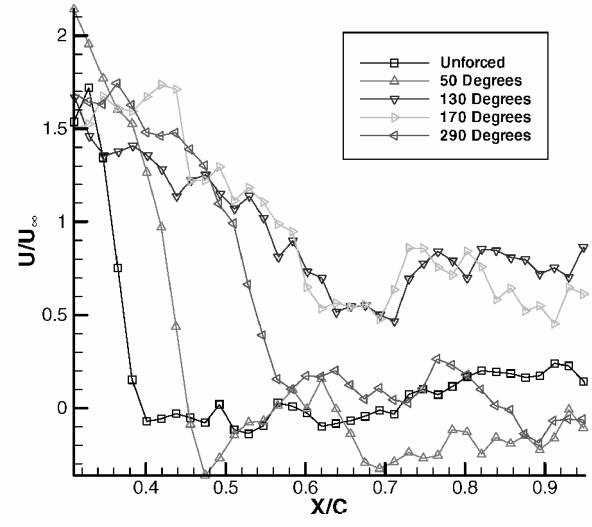

Fig. 14 Experimental axial velocity development along the vortex core.

Figure 17 shows the normal force acting on the delta wing. Initially the PSB is turned off (unforced case), and at approximately 29,800, iterations the PSB is initiated. There are a variety of interesting details that can be seen when comparing the two cases. As the PSB is initiated, the average normal force acting on the delta wing increased from 0.945 to 0.987 N, just under a 5% increase in normal force. In addition, the unforced case has a fairly low primary nondimensional frequency of $F^+ = 0.221$, which is caused by the winding of the burst vortex. The primary frequency increases to $F^+ = 1.75$ when the PSB is initiated, which is the frequency of the suction and blowing. Whereas the forced case seems to provide improved lifting characteristics (on the average), in fact the fluctuations in normal force also increase as the suction and blowing is initiated. Peaks in normal force as high as 1.15 N can be seen in Fig. 17, but valleys as low as 0.8 N are also visible. Whether this represents an improvement in wing lifting characteristics is open to debate. The highly oscillatory nature of the forced case might make PSB impractical for everyday use unless some method for controlling the force variations is determined.

The double frequencies for the converged PSB case are easily seen in Fig. 18, which shows the normal force variation for 17,000

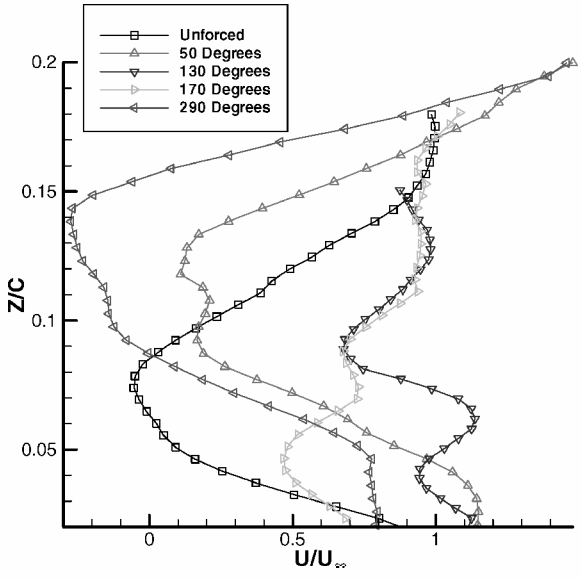

Fig. 15 Experimental axial velocity profiles at $x/c = 0.6$.

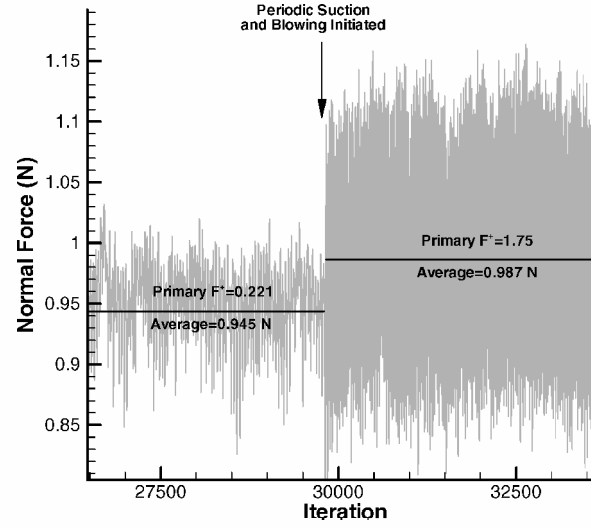

Fig. 17 Normal force variation as periodic suction and blowing is initiated.

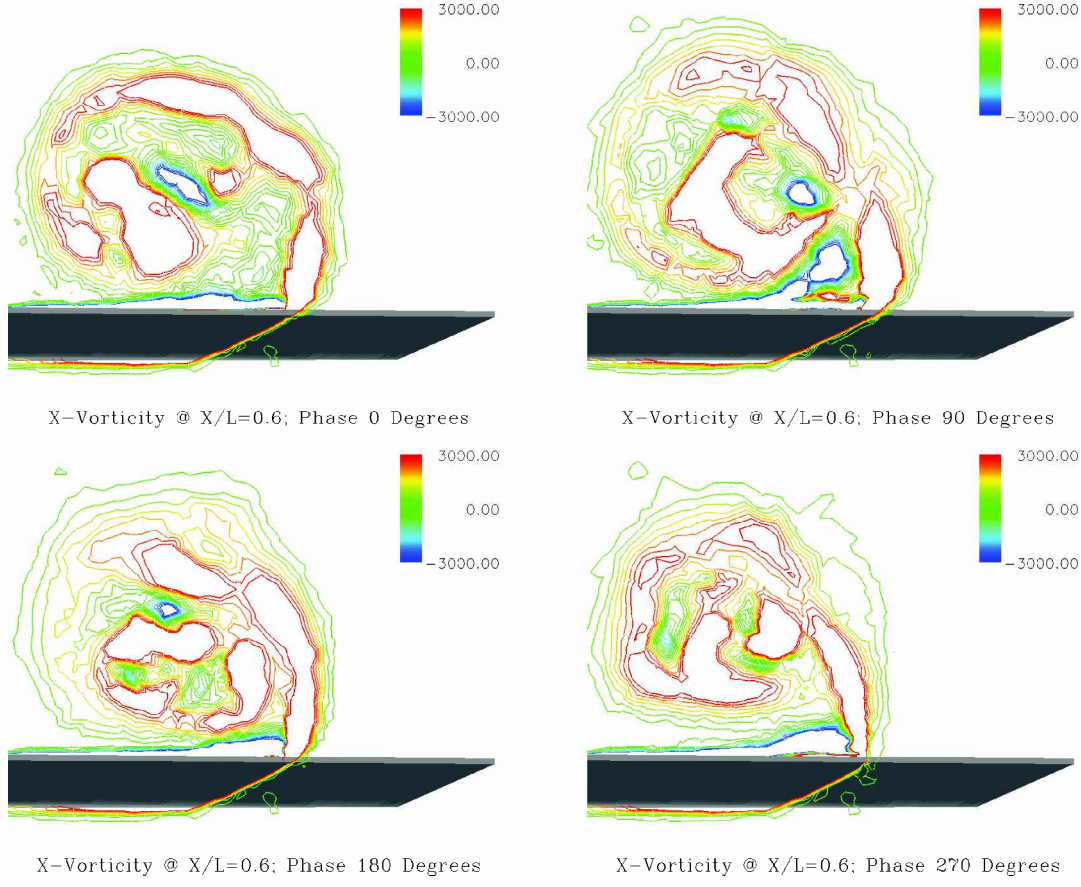

Fig. 16 Computational prediction of vortex during the forcing cycle, $x/c = 0.6$.

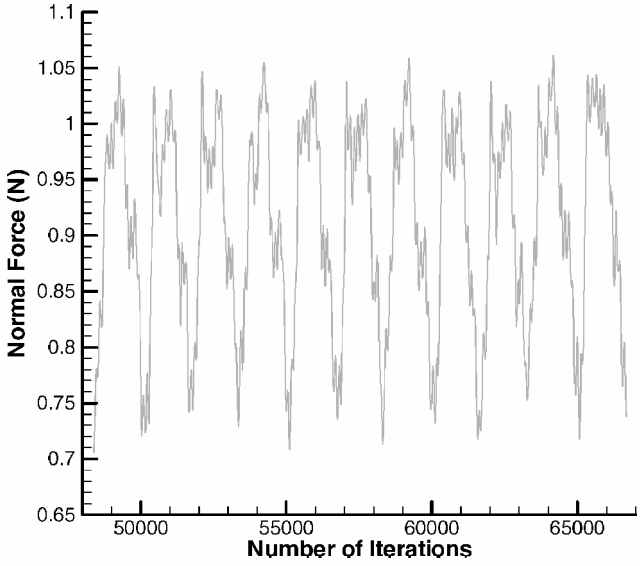

Fig. 18 Normal force variation for PSB, $\Delta t^* = 0.006$.

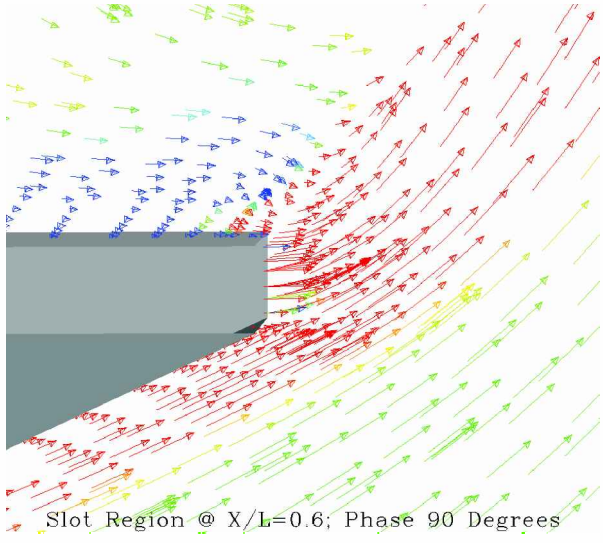

a) Blowing phase

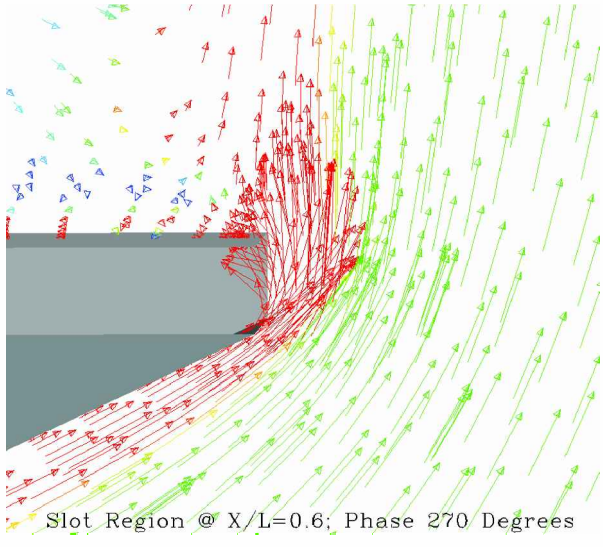

b) Suction phase

Fig. 19 Velocity vectors in the vicinity of the slot colored by x vorticity, $x/c = 0.6$.

iterations (over 10 cycles of the suction and blowing). Both the suction and blowing frequency is obvious, but overlayed on that frequency is the shear layer instability frequency, constantly oscillating around the lower frequency. The average normal force is now 0.921 N, which is even lower than the unforced case. This difference may be due to the different time steps used and should not be used to draw conclusions. Notice that the blowing portion of the suction/blowing cycle is more effective, as evidenced by the amount of time the normal force remains at the highest levels. When the suction cycle takes place, decreasing the normal force, the force spikes to a minimum value but then quickly rises again as the suction phase ends. This explains why, during the experimental portion of this work, it appeared that the suction was incomplete (or possibly working incorrectly). Even the numerical simulation clearly shows that the suction phase is not as effective in altering the normal force acting on the delta wing.

Closeups of the flowfield in the vicinity of the slot help to explain the results of Fig. 18. Figure 19 shows velocity vectors colored by x vorticity for two phases of the PSB cycle. It is clearly evident that the blowing phase is affecting a large change to the velocity field in the vicinity of the slot, whereas the suction phase is not nearly as affective. This is probably due to the difficulty the suction has in forcing the crossflow to turn the corner into the slot, whereas the blowing is enhancing the upward direction of the crossflow. In fact, the suction seems to turn more air upward than into the slot. Future slot configurations should take this into account.

Conclusions

The flow over a 70-deg delta wing at a chord Reynolds number of 4.07×10^4 and an angle of attack of 35 deg was investigated in a water-tunnel experiment and by a numerical simulation. The flow was forced using PSB along the entire leading edge at a nondimensional frequency of $F^+ = 1.75$. It was found that PSB does not delay vortex breakdown a great deal, with vortex breakdown taking place between $x/c = 0.4$ and 0.5 for both the forced and unforced case, as evidenced by a drop in vorticity by almost an order of magnitude. For the unforced flow, the location of the drop in streamwise vorticity was found to coincide with a drop in axial velocity. For the forced flow, the location where the axial velocity dropped abruptly was fluctuating throughout the forcing cycle between $x/c = 0.45$ and downstream of the trailing edge. The forcing resulted in an overall increase in axial velocity in the vortex core near the wing surface, especially beyond vortex breakdown.

Because forcing does not appear to improve the flow upstream of vortex breakdown, future experiments are planned to investigate the effect of forcing along portions of the leading edge instead of the entire leading edge. Also, forcing methods that may improve the location of vortex breakdown by altering the shape of the vortex core from straight to curved by using spatially modulated forcing upstream of the natural vortex breakdown location are being considered.

A critical examination of the results obtained from a numerical simulation of the flowfield on a delta wing with PSB was also presented. The results indicate that the computational scheme properly captured the effect of PSB on the main parameters of the flowfield and on the normal force of the delta wing. The numerical results enabled the researchers to investigate a variety of flowfield details that were not known from the experiments, including the frequency of the vortex breakdown winding, the incremental change in normal force on the delta wing due to PSB, the oscillatory behavior of the force acting on the delta wing, and the impact of the PSB on the burst vortex winding frequency. In addition, the numerical simulation was suggested as a method to verify difficulties in the experiment, such as the possibility of the suction cycle not being fully realized.

A great deal of value can be achieved when experiments and computations are used in a synergistic fashion. Each approach has its strengths and weaknesses, and by employing the strengths of both experiments and computations in solving an aerodynamic problem, a more complete and full picture of the processes of aerodynamics will be more realized.

References

[1]Ekaterinaris, J. A., Coutley, R. L., Schiff, L. B., and Platzer, M. F., "Numerical Investigation of High Incidence Flow Over a Double-Delta Wing," *Journal of Aircraft*, Vol. 32, No. 3, 1995, pp. 457–463.

[2]Murman, S., Rizk, Y. M., Cummings, R. M., and Schiff, L. B., "Computational Investigation of Slot Blowing for Fuselage Forebody Flow Control," *Aircraft Design*, Vol. 2, No. 1, 1999, pp. 45–63.

[3]Huang, X. Z., Lui, T. C., and Hanff, E. S., "A Novel Concept for Controlling Leading-Edge Vortex Breakdown and Related Preliminary Water Tunnel Experiment," AIAA Paper 2001-4143, Aug. 2001.

[4]Mitchell, A. M., and Delery, J., "Research Into Vortex Breakdown Control," *Progress in Aerospace Sciences*, Vol. 37, No. 4, 2001, pp. 385–418.

[5]Mitchell, A. M., Barber, D., Molton, P., and Delery, J., "Oscillation of Vortex Breakdown Location and Blowing Control of Time-Averaged Location," *AIAA Journal*, Vol. 38, No. 5, 2000, pp. 793–803.

[6]Visbal, M. R., "Computational and Physical Aspects of Vortex Breakdown on Delta Wings," AIAA Paper 95-0585, Jan. 1995.

[7]Agrawal, S. A., and Barnett, R., "Numerical Investigation of Vortex Breakdown on a Delta Wing," *AIAA Journal*, Vol. 30, No. 3, 1992, pp. 584–591.

[8]Iwanski, K. P., Ng, T. T., and Nelson, R. C., "An Experimental Investigation of Delta Wing Vortex Flow With and Without External Jet Blowing," AIAA Paper 89-0084, Jan. 1989.

[9]Guy, Y., Morrow, J. A., and McLaughlin, T. A., "Control of Vortex Breakdown on a Delta Wing by Periodic Blowing and Suction," AIAA Paper 99-0132, Jan. 1999.

[10]Guy, Y., Morrow, J. A., McLaughlin, T. A., and Wygnanski, I., "Pressure Measurement and Flow Field Visualization on a Delta Wing with Periodic Blowing and Suction," AIAA Paper 99-4178, Aug. 1999.

[11]Guy, Y., Morrow, J. A., McLaughlin, T. A., and Wygnanski, I., "Parametric Investigation of the Effects of Active Control on the Normal Force on a Delta Wing," AIAA Paper 2000-0549, Jan. 2000.

[12]Guy, Y., Morrow, J. A., McLaughlin, T. A., and Wygnanski, I., "Velocity Measurements on a Delta Wing with Periodic Blowing and Suction," AIAA Paper 2000-0550, Jan. 2000.

[13]Morton, S. A., Guy, Y., Morrow, J. A., and Blake, D. C., "Numerical Simulation of Periodic Suction and Blowing Control of Vortex Breakdown on a Delta Wing," AIAA Paper 99-3195, June 1999.

[14]Siegel, S. G., McLaughlin, T. E., and Morrow, J. A., "PIV Measurements on a Delta Wing with Periodic Blowing and Suction," AIAA Paper 2001-2436, June 2001.

[15]Strang, W. Z., Tomaro, R. F., and Grismer, M. J., "The Defining Methods of $Cobalt_{60}$: A Parallel, Implicit, Unstructured Euler/Navier–Stokes Flow Solver," AIAA Paper 99-0786, Jan. 1999.

[16]Tomaro, R. F., Strang, W. Z., and Sankar, L. N., "An Implicit Algorithm for Solving Time Dependent Flows on Unstructured Grids," AIAA Paper 97-0333, Jan. 1997.

[17]Grismer, M. J., Strang, W. Z., Tomaro, R. F., and Witzemman, F. C., "Cobalt: A Parallel, Implicit, Unstructured Euler/Navier–Stokes Solver," *Advances in Engineering Software*, Vol. 29, No. 3–6, 1998, pp. 365–373.

[18]Forsythe, J. R., Strang, W., Hoffmann, K. A., "Validation of Several Reynolds-Averaged Turbulence Models in a 3D Unstructured Grid Code," AIAA Paper 2000-2552, June 2000.

[19]Morton, S. A., Guy, Y., Morrow, J. A., and Blake, D.C., "Numerical Simulation of Periodic Suction and Blowing Control of Vortex Breakdown on a Delta Wing," AIAA Paper 99-3195, June 1999.

[20]Guy, Y., Morton, S. A., and Morrow, J. A., "Numerical Investigation of the Flow Field on a Delta Wing with Periodic Blowing and Suction," AIAA Paper 2000-2321, June 2000.

[21]Cummings, R. M., Morton, S. A., Siegel, S. G., McLaughlin, T. E., and Albertson, J. A., "Combined Computational Simulation and PIV Measurements on a Delta Wing with Periodic Suction and Blowing," AIAA Paper 2002-0300, Jan. 2002.

[22]Barberis, D., Quelin, C., and Petit, S., "Contrôl de L'éclatement Tourbillonnaire Sur L'aile AFV-D60° au Tunnel Hydrodynamique TH2," ONERA, Technical Rept. RT 136/03582 DAFE, March 2001.

[23]Gad-el-Hak, M., and Blackwelder, R. F., "The Discrete Vortices From a Delta Wing," *AIAA Journal*, Vol. 23, No. 6, 1985, pp. 961, 962.

[24]Lowson, M. V., "The Three Dimensional Vortex Sheet Structure on Delta Wings," Fluid Dynamics of Three-Dimensional Turbulent Shear Flows and Transition, CP-438, AGARD, Oct. 1988, pp. 11.1–11.16.

[25]Cummings, R. M., Morton, S. A., and Siegel, S. G., "Computational Simulation and PIV Measurements of the Laminar Vortical Flowfield for a Delta Wing at High Angle of Attack," AIAA Paper 2003-1102, Jan. 2003.

Color reproductions courtesy of U.S. Air Force Academy.